

RESEARCH ARTICLE OPEN ACCESS

Mechanical Fatigue in Liquid-Metal Interconnects: Failure Mechanism Analysis and Validation of Improvement Strategies

Lennert Purnal¹  | Maximilian Krack^{1,3}  | Parth Vinayakrao Sewlikar^{1,2} | Bart Ruttens^{1,3} | Tom Hauffman^{1,2}  | Iris De Graeve^{1,2}  | Wim Deferme^{1,3}  | Michaël Daenen^{1,3}  | Monika Rai^{1,3}

¹Hasselt University, Institute for Materials Research, Hasselt, Belgium | ²Materials and Chemistry, Sustainable Materials Engineering, Vrije Universiteit Brussel, Elsene, Belgium | ³IMEC vzw, Division IMOMEC, Diepenbeek, Belgium

Correspondence: Lennert Purnal (lennert.purnal@uhasselt.be) | Michaël Daenen (michael.daenen@uhasselt.be)

Received: 9 October 2025 | **Revised:** 2 December 2025 | **Accepted:** 4 December 2025

Keywords: destructive testing | failure mode and mechanisms | liquid metals | strain relief | stretchable electronics reliability

ABSTRACT

Stretchable electronics that combine mechanical compliance with reliable electrical performance are essential for applications in soft robotics, wearable systems, and healthcare monitoring. Among the available conductive materials, liquid metals (LMs) offer exceptional conductivity and intrinsic deformability when encapsulated in elastomers, yet the long-term reliability remains a challenge. This work addresses the critical issue of robust interconnections between the LM and rigid or flexible components, where stress concentration leads to failure under repeated strain. Herein, the robustness of such interfaces is improved by first eliminating secondary failure modes, such as silicone rupture and short circuits, until connection failure is the final dominant mode. Targeted connector designs are introduced to improve connection stability. Through X-Ray tomography, delamination between encapsulant and connector is identified as the primary failure mechanism, which is subsequently mitigated through material based strain relief around the LM-solid interface. Devices incorporating this strategy withstand at least one million cycles at 50% strain, even when rigid components are integrated. Further, at 100% strain, the cyclic durability increases from 16% survival rate to 50% survival rate after 100 000 stretch cycles by applying strain relief. These findings establish a framework for reliable LM-based stretchable interconnections in demanding applications.

1 | Introduction

Over the past decade, there has been a growing interest in electronic systems that can seamlessly deform, bend, and stretch while maintaining reliable electrical connection [1]. Such stretchable electronics open the door to a wide range of emerging applications, including soft robotics [2], wearable [3] and implantable healthcare devices [4, 5], and human machine interfaces [6], where electronic components must withstand large deformations without failure. In these domains, two requirements are particularly critical: the ability to withstand large mechanical

strains, often up to 50%, and to maintain long-term electrical stability under repeated cyclic loading at those strains. These demands place stringent constraints on both materials and interconnection strategies.

Among the various materials investigated for stretchable conductors, liquid metals (LM) particularly gallium based alloys have emerged as a promising solution [7–9]. Unlike solid metallic films or conductive composites, LMs offer metallic-level conductivity with intrinsic fluidic deformability, enabling interconnects that can stretch, flex and compress without plastic deformation

or fracture [10]. When encapsulated within soft elastomers, LM traces can sustain extreme strains while preserving stable electrical pathways, making them especially attractive for next-generation stretchable electronic systems.

To give real functionality to devices, the LM traces must always be connected to flexible or solid connectors and components to provide power, communication, measurements, or other functionality. This transition from liquid to solid is usually the bottleneck in terms of reliability due to the high stress concentrations at the interface [11, 12]. Thus, reliably interconnecting LM to components and connectors remains a significant challenge. Conventional methods for mounting components and connectors are either not compatible, such as soldering, or not practical, such as embedding wires [13]. A common method to interconnect LMs to components or the outside world is by using flexible printed circuits (FPC) as a connector or intermediate medium [12, 14–18]. Moreover, the first commercial LM-based stretchable electronics also use an FPC to connect to the traces [19]. Despite this, analysis of the stability, longevity and failure mechanisms of these interfaces under mechanical loading remains superficial.

While there are studies analyzing the overall reliability of LM-based interconnects under diverse mechanical loads (e.g., extension, bending, torsion, vibrations, high temperature), they largely focus on bulk conductor behavior rather than dissecting failure modes at the interface with rigid or flexible components [20]. This is usually because the devices are not tested up to failure and thus no failure mechanisms can be studied. Conversely, if failure is reached, subsequent analysis of the cause is often lacking.

Moreover, mechanical instabilities, such as leakage in high LM-content composites or fracture at mounting points during high strain have been observed and highlight structural challenges [14]. Again, these tend to focus on the composite itself rather than on the interface with components.

In broader flexible electronics, interfacial failure, including delamination between rigid chips and bendable substrates, is well documented as a primary cause of device failure under mechanical loading. The use of strain relieving structures and Young's modulus gradient in stretchable electronics using LM or other stretchable conductors [21–23] has been shown. However, when specifically dealing with LM interconnects, there remains a notable gap in the literature regarding systematic, failure mode focused studies of the metallic liquid–solid interface. Further, statistically relevant proof of the effectiveness of strain relief in cyclic mechanical loading is lacking in literature, which stems from the need to go to a high amount of cycles to reach failure. Researchers have leveraged connector geometry [12, 17], material transitions [18, 24] or encapsulant geometry [25] to create strain relief. Single stretch tests have shown their functionality. However, the effectiveness has not been shown in cyclic mechanical fatigue tests, especially with statistical proof.

Therefore, the key gap lies in the absence of detailed, interface-level investigations that pinpoint how and where failures originate: whether from mechanical stress, delamination, oxidation, poor adhesion, or other mechanisms, and how these phenomena evolve under realistic loading conditions.

In this work, we address the critical challenge of solid–liquid interconnections in LM-based stretchable electronics by evaluating their mechanical and electrical reliability under large strains and long-term cyclic loading. The main goal is to provide a systematic approach to evaluate such interconnections and improvement strategies. To do so, custom test structures were designed, inspired by standardized elastomer testing geometries. To interface the liquid metal conductors with conventional electronics, two flexible printed circuit (FPC) connector geometries were designed and compared. Furthermore, the use of batch fabrication techniques ensured statistically meaningful comparisons across sample groups, allowing failure distributions and dominant mechanisms to be identified. A custom-built cyclic stretch testing setup, coupled with four probe resistance measurements, enabled monitoring of the cyclic degradation and resulting failure modes by testing up to failure. Once the failure modes (e.g., encapsulant rupture, electrical disconnect, or short-circuit) have been identified, their underlying mechanism is studied (e.g., crack initiator, LM oxidation, delamination causing flow, etc.). Using this setup, targeted improvements such as connector design optimization and strain relief on components were tested and verified. This approach establishes a systematic methodology to investigate and quantify failure mechanisms at the solid–liquid interface. A guideline on the mitigation and improvement of the failure modes encountered in the base sample design is presented and validated on a revised architecture with an integrated LED, leading to devices that maintain stable performance over a million cycles at 50% strain.

2 | Materials and Methods

2.1 | Sample Design

The physical stack of the devices consists simply of an encapsulating stretchable material in which channels of LM interconnect multiple rigid components and/or flexible connectors (FPCs). The stretchable material has to fully encapsulate the LM traces in order to prevent leakage and flow.

As there are currently no established standards for testing highly stretchable electronic systems, particularly those capable of enduring strains exceeding 100%, custom sample designs were developed to enable reliable, repeatable mechanical and electrical characterization. Here, the design decisions are clarified.

To prevent tearing of the silicone substrate during stretching, the sample geometry was inspired by standardized testing methods for elastomeric materials, notably the use of a dogbone-shaped structure as shown in Figure 1a was based on ASTM D412 [26]. This shape helps to concentrate strain in a controlled region and minimizes stress concentrations near clamping points.

The samples were designed with full symmetry to eliminate asymmetric mechanical forces that could influence the behavior of individual components or connections during stretching. While the symmetrical design introduces added complexity during the fabrication, particularly in the precise alignment of connectors on both ends, it enhances the realism of the setup by mimicking multicomponent stretchable systems where such alignment is critical.

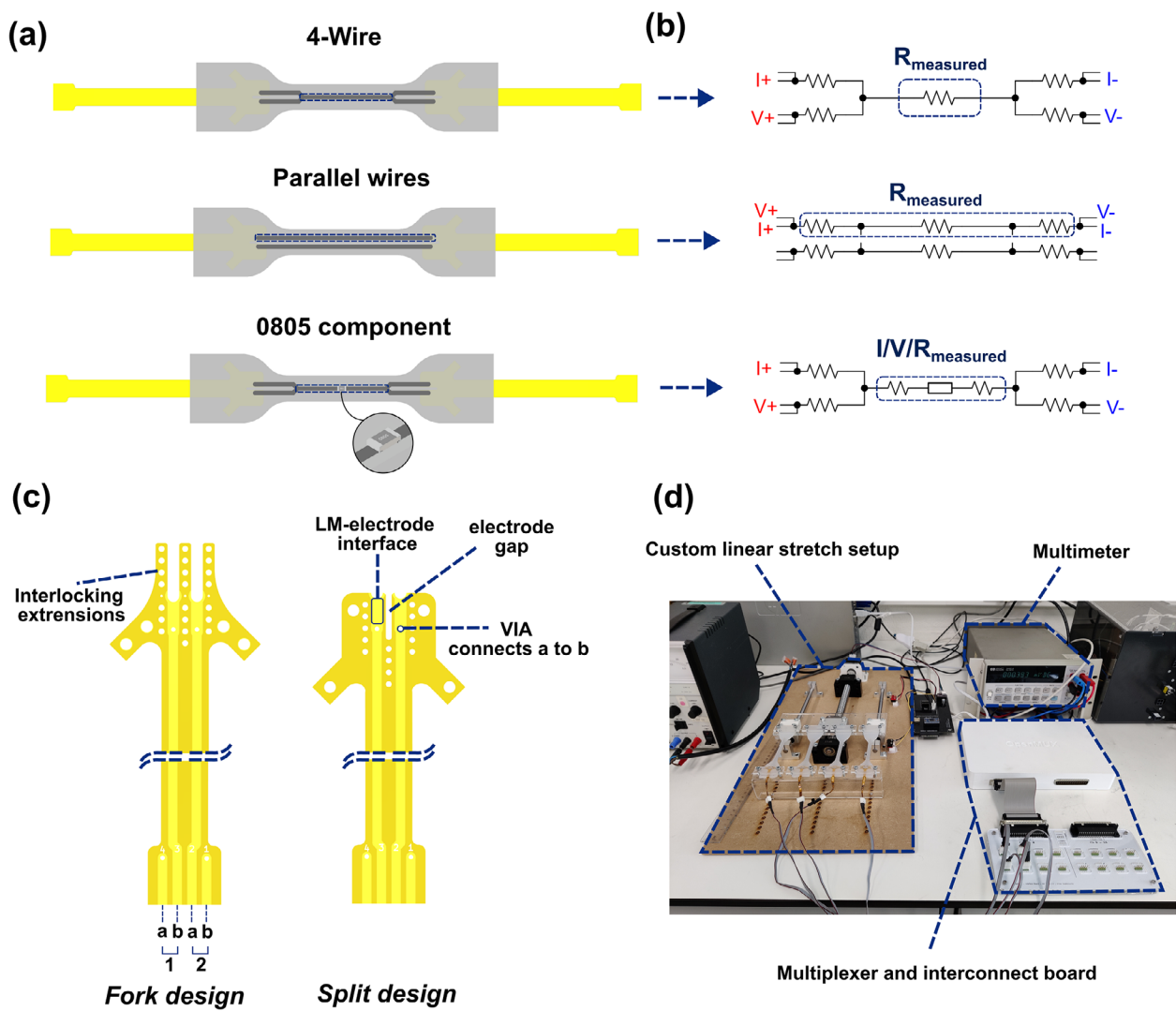


FIGURE 1 | (a) Dogbone shaped sample designs with 3 distinct measurement functions: “4-wire” for LM trace investigation, “Parallel wires” for connections and “0805 component” for small rigid electronic components. (b) Equivalent electrical schematics for designs from Figure 1a. (c) Schematics of the “Fork” and “Split” connector designs. (d) Custom parallelized cyclic stretch setup with linear stretch bench, multimeter, multiplexer and interconnect board.

In this work, 3 distinct sample designs were developed to focus the electrical measurement on different components. As illustrated in Figure 1a,b, there is a “4-Wire” design, a “Parallel wires” design and a “0805 component” design. All devices incorporate 1 mm wide traces, defined by stencil openings during fabrication. The use of two neighboring interconnects spaced 1mm apart allows for the investigation of interconnect integrity and the potential for short circuits during mechanical deformation. This aspect is essential for understanding failure mechanisms in practical systems where multiple conductors may be routed in close proximity.

The 4-Wire design has a single liquid metal trace in the center of the device, and is connected through 4 liquid metal traces to the FPC and in turn to the outside measurement equipment. As such, the measurement can be focused on the center wire without the influence of the connector resistances. This design can thus be used to measure the reliability and resistance change of the liquid metal only. Care has been taken to place the center wire entirely in

the uniformly stretching section of the dogbone shape to improve the predictability of the resistance change. That required longer interconnect traces, which in turn allows more flow of LM from the center trace to the outer traces. This trade-off has to be taken into account.

The “Parallel wires” design has 2 separate straight LM traces that connect from one end of the sample to the other. The FPC connector design still allows for a 4-wire measurement that minimizes the influence of test cable leads. In this design, the measurement is focused on the FPC to LM connections and the wires. The inclusion of this connection allows for monitoring the degradation of the solid-liquid interface that would not be captured in the “4-Wire” design. Finally, the use of 2 wires doubles the amount of usable data per sample, which is beneficial in long-term durability tests. A comparison of the resistance vs. strain response between the “4-wire” design and “parallel” wires design in Figure S1 shows the effect of the constant contact resistance that reduces the gauge factor of the “parallel wires” design.

Lastly, the “0805 component” design is similar to the “4-wire” design but incorporates an 0805 package surface mount component in the center. In this research, an LED is used to test the failure. Similar to the 4-wire design, a constant current (20 mA) is passed through the device using two probes and the other two are used to measure voltage. This way, an open circuit and a short circuit (between anode and cathode of the LED) can be differentiated by the measurement of 21 V(multimeter compliance limit) or 0 V, respectively. Under normal operation, the working voltage of the LED at 20 mA current should be measured. Additionally, the LED gives visual feedback of its function.

To interface the stretchable LM region with conventional electronics, two flexible printed circuit board (FPC) connector designs were developed and compared as shown in Figure 1c: a fork design and a split design. Both connector types are fabricated on polyimide substrates and feature four input terminals on the rigid (instrumentation) side and two output terminals interfacing with the liquid metal. Internally, each pair of input terminals is shorted together near the output by a plated-through VIA, enabling four probe resistance measurements that capture the solid-to-liquid interconnection resistance. This measurement approach is crucial for accurately assessing the solid-to-liquid interconnection stability under strain.

The Fork design is based on previous patented technology [27] and incorporates mechanical stabilization fingers extending around the output pads both on the outer sides and between them. These fingers are embedded within the encapsulant, provided there is sufficient adhesion, to restrict motion of the LM at the interconnection site. The primary goal is to improve mechanical stability around the transition zone between rigid and stretchable components.

The Split design features a void region between the output pads, creating a gap into which the encapsulant can flow. This forms a physical barrier between adjacent LM traces, helping to mitigate the risk of short circuits due to LM flow during deformation. However, this comes at the expense of mechanical stability, as there are fewer anchor points near the interconnection to restrict movement.

2.2 | Test Setup

The test setup for cyclical testing, as shown in Figure 1d consists of 4 main components: The cyclic stretcher, the multimeter(s), multiplexer(s) and a computer (raspberry pi) to coordinate the movements and measurements.

The custom linear stretch setup consists of a spindle-type system that translates the rotary movement of a motor into linear movement for stretching. Using clamps with a fixed height of 2 mm, the indentation of the samples at the clamps is kept constant. Four samples can be simultaneously clamped in a stretcher. However, the custom software allows for multiple stretchers to be connected simultaneously.

The 4-wire measurement is performed using an HP 3458A multimeter. A multiplexer is used to switch the measurement

between samples. In cyclic tests, this does not allow for fast and continuous measurements of all samples during stretching simultaneously, but is required to improve sample throughput. Instead, a measurement is performed on each sample at the minimum extension (0% strain) and maximum extension of the stretch cycle. The samples are measured every cycle for the first 100 cycles to gain extra detail on the initial resistance change. After this, to further speed up the test, the samples are measured every 10 cycles, which still gives information on the trend in resistance change and sample failure.

2.3 | Fabrication Procedure

To ensure statistical significance in evaluating the reliability of the interconnections, a reproducible and consistent batch production method was developed. This process enables the fabrication of a sufficiently large and uniformly distributed amount of test samples, allowing for a robust comparison of performance metrics and failure distributions.

Each batch consists of eight simultaneously fabricated samples, as shown in Figure S2. The illustrations in Figure 2 shows a single sample in fabrication. The production process begins with the preparation and positioning of the FPC connectors, which are first coated with a toluene-free Wacker G790 primer to promote adhesion with the encapsulant. The FPCs are then mounted to a PMMA baseplate using a water-washable, PVA-based adhesive, with the contact pads facing the baseplate as shown in Figure 2a. Precise placement is ensured by engraved alignment markers on the baseplate to guide the orientation and position of each connector and component.

Next, the first mold half, shaped to define the first encapsulant layer, is aligned and mounted onto the baseplate like in Figure 2b. The first encapsulation layer of silicone is then overmolded onto the FPCs via manual injection using a syringe (Figure 2c). The encapsulant material is a two-component, platinum-cure silicone (Ecoflex 00-30), chosen for its mechanical flexibility and stretchability, and its low viscosity to facilitate the injection. To ensure uniformity and to avoid voids, the silicone is mixed using a centrifugal speed mixer (Hauschild speedmixer DAC400) at 2000 rpm for 1 min and vacuum degassed for 20 min prior to injection. This step is critical to eliminate air bubbles, which could otherwise act as stress concentrators and lead to premature mechanical failure under strain, as explained later in 3.1.

Curing is performed in an oven at 50°C for 30 min to accelerate cross-linking. Prior to use, the mold surface in contact with the silicone was mechanically roughened using 300-grit sandpaper, which promotes stronger adhesion between the cured silicone and the mold surface. This ensures that the encapsulated FPCs remain embedded in the mold when the baseplate is removed after curing.

Next, the stack is flipped, and the baseplate is removed, exposing the component and connector pads on the surface (Figure 2d). The surface is cleaned with DI water to remove the remaining adhesive. As shown in Figure 2e, a laser-cut PET stencil with apertures in the shape of the desired conductive traces is carefully aligned and placed on top of the cured samples. The LM is applied

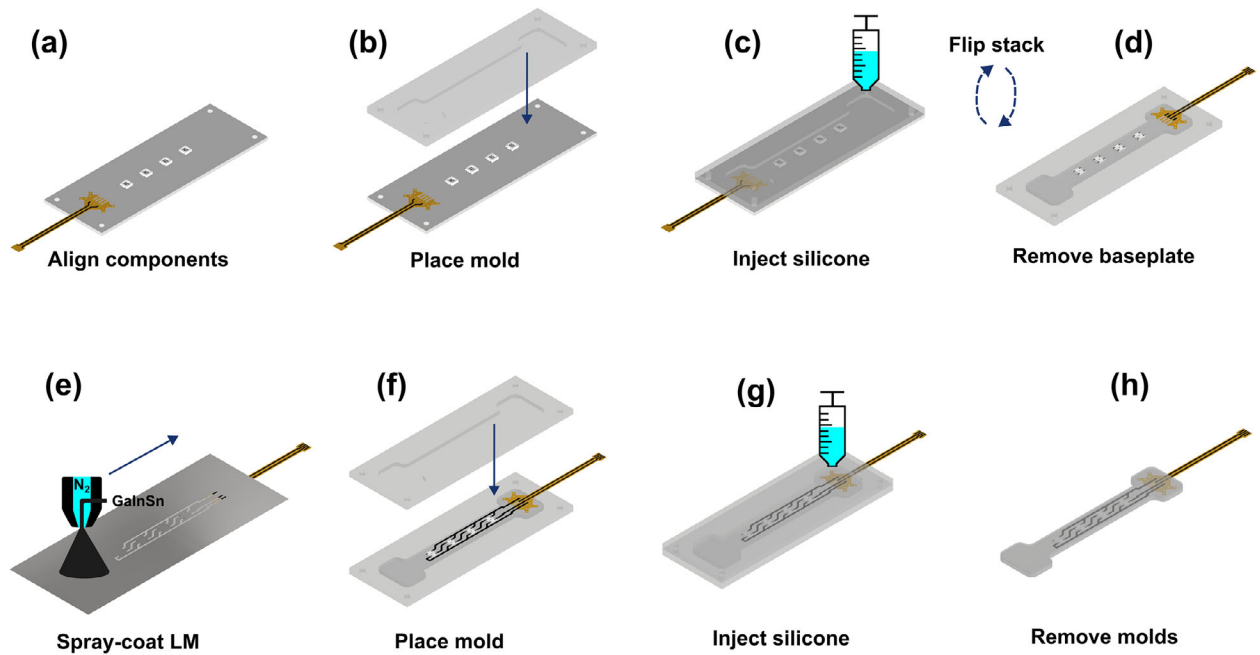


FIGURE 2 | (a) Components are aligned and mounted to the baseplate using washable PVA adhesive. (b) PMMA mold preparation. (c) Liquid silicone rubber injection. (d) Baseplate is removed, exposing the electrical contacts. (e) Stencil is aligned and placed, after which LM is spray coated by a custom automated spray coater. (f) Stencil is removed, and next layer mold is placed. (g) Silicone is carefully injected over the LM traces. (h) Mold removal exposes final device.

using a custom-built spray-coating system. Spray-coating of the LM was performed in ambient laboratory conditions (20–25°C) by scanning a single pass in a raster pattern over the substrate at 25 mm per s, with 3.5 bar nitrogen gas, a LM flow rate of 1 mL per min, and a spray height of 15 cm. These parameters were optimized to achieve a uniform, low-roughness LM layer with high electrical conductivity. Details regarding the spray-coater setup and performance characteristics of the deposited LM traces are described in detail in [28]. The use of spray-coating removes the need for pre or post treatment of the contacts [29] because the impact of the LM droplets ruptures the oxide, providing sufficient electrical contact [30].

Following deposition, the stencil is removed, leaving behind precisely patterned LM interconnects. The upper mold half, shaped to define the second encapsulant layer, is then mounted (Figure 2f), and a final layer of Ecoflex 00-30 (EF30) is carefully injected over the LM traces (Figure 2g). During this step, injection is performed slowly and with minimal pressure to avoid disturbing the patterned LM. Finally, the samples can be removed from the mold (Figure 2h). This two-stage molding approach ensures a flat and uniform base surface for LM spraying and a consistent top encapsulation layer, yielding highly repeatable and reliable samples for mechanical and electrical testing with consistent dimensions.

3 | Results and Failure Analysis

3.1 | Observed Failure Modes

Initial testing of early sample designs revealed multiple potential failure modes during cyclic stretching. These included delamination

of the encapsulant, rupture of the silicone matrix, electrical short circuits between adjacent traces, and loss of electrical connectivity at the solid-liquid metal interface. In this section, targeted design and process modifications were implemented to eliminate or mitigate the influence of secondary failure sources. In this way, the final dominant failure mode and its mechanism is studied and mitigated.

First, encapsulant delamination, typically initiated at the interface between successive silicone layers, was effectively eliminated by improving interlayer adhesion. In the case of EF30 based devices, this is done by limiting the time between casting successive layers to 1 h after curing. As such, the present encapsulant layer is still reactive enough for the next layer to bond with.

3.1.1 | Silicone Rupture

Mechanical failure of the encapsulant, particularly rupture during cyclic or high-strain loading, is mainly caused by crack initiators such as air cavities that are present in the stretchable matrix [31]. Such bubbles can rupture due to excessive strain or can gradually rupture with cyclic strain. In the latter case, this is visible in the resistance measurement (Figure 3a) where a sudden sharp increase happens over a short amount of cycles after the bubble starts rupturing. After this point, the crack grows each cycle, sharply increasing the length locally and thus increasing the resistance following Pouillet's law until it fully breaks the trace or the sample. This phenomenon was addressed by minimizing air cavity formation during fabrication by vacuum degassing the EF30 silicone prior to injection, thereby reducing internal voids that can act as stress concentrators under deformation. Additionally, sharp edges in the sample design

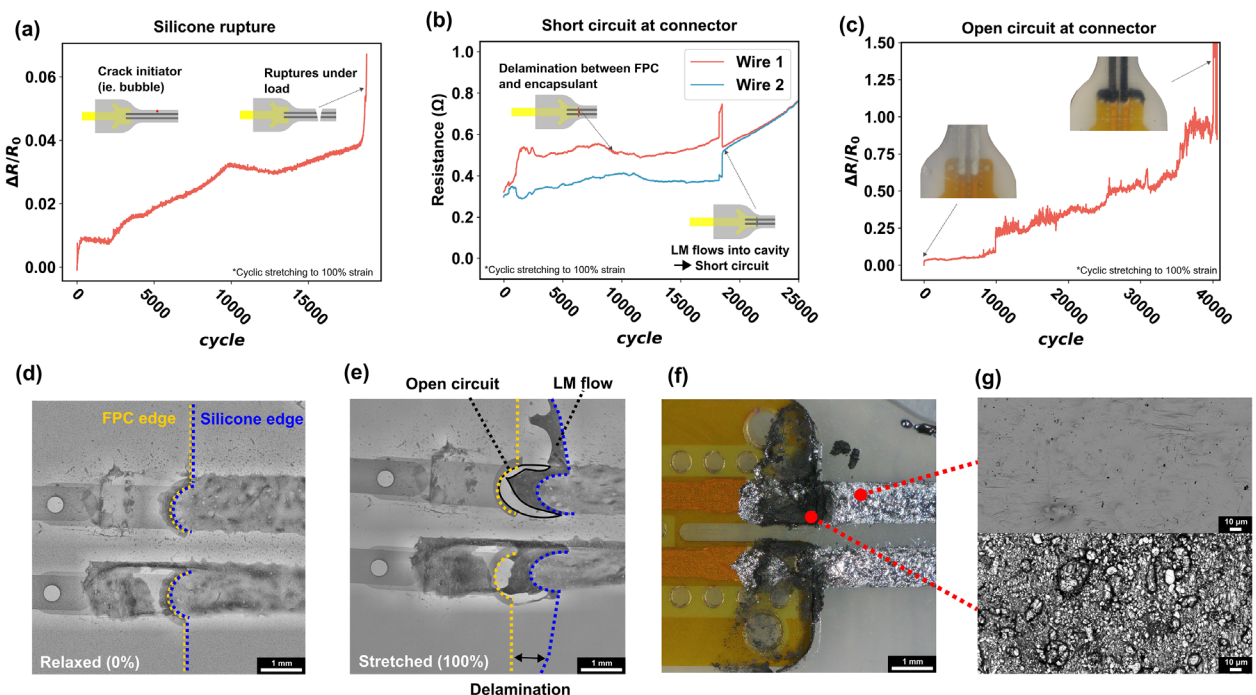


FIGURE 3 | (a) Example of the resistance change of a device that fails due to the encapsulant rupturing and breaking the LM channel. (b) Example of the resistance of two adjacent wires becoming the same after a short circuit at the connector. (c) Example of unstable resistance response due to delamination of the encapsulant and connector, causing LM flow, finally resulting in open circuit. (d,e) X-ray tomography images of a fully encapsulated sample that failed due to an open circuit, caused by a gap between wire and connector pad due to delamination. Yellow dashes show the FPC connector edge. Blue dashes show the corresponding silicone edge and how it moved due to delamination. (f) Post-mortem optical microscopy image of a device at the connector where the top encapsulation was removed. (g) SEM backscattered micrographs of the LM in the trace (top) and the degraded LM on the connector (bottom).

should be avoided as these can also initiate rupture. The dogbone-shaped sample design already accounts for this. Furthermore, internal components, connectors, or other inclusions can also be seen as possible crack initiators and must be placed strategically.

3.1.2 | Short Circuits

Short circuits between adjacent liquid metal traces, caused by lateral flow or merging of the LM wires during stretching are another possible failure mode. The main mechanism is that due to the mechanical mismatch between the connector and the encapsulant, they delaminate between the pads. Thus, a cavity is created between the connector pads, which is consequently filled by the LM from the traces, connecting them electrically. As shown in Figure 3b, this was measured using the “Parallel wires” design. The measured resistance of both traces becomes equal (both resistances in parallel) when the traces short circuit at the connections on both ends. The introduction of the split connector design, featuring a void section between adjacent pads, resolves this issue. During fabrication, the liquid silicone rubber fills the gap between the pads and effectively creates a barrier against flow between the traces, even when delamination occurs.

3.1.3 | Connection Failure

After these failure modes were systematically addressed and eliminated through design and process optimization, a single

dominant failure mode remained consistent across all test samples: electrical open-circuit at the solid-liquid interface, specifically at the junction between the LM and the polyimide-based FPC connector.

This failure was observed under both monotonic and cyclic strain conditions and was identified as the primary limitation to interconnect reliability in the current system. Electrical disconnection was marked by a sharp rise in resistance or open-circuit behavior (see Figure 3c), despite the LM traces and encapsulant remaining visually intact. This indicates that the mechanical and electrical integrity of the solid-liquid interface is the most critical factor governing long-term device performance and is therefore the focus of the subsequent failure mechanism analysis and mitigation strategy in this work.

The primary cause of the connection loss at the interconnection is due to the mechanical mismatch between the stretchable encapsulant and the rigid/flexible connector, similar to the short circuit mechanism. This causes high stress concentrations, specifically at the sharp edge of the FPC. Excessive strain or cyclic strain then causes the encapsulant to instantly or gradually delaminate from the FPC at the edge if the adhesion strength is exceeded, creating a void/gap as shown in Figure 3d,e. Initially, LM is allowed to flow in these cavities, which can be seen by the black deposit around the connector. This is also visible in the resistance response, where the geometric change of the LM channel caused the flow into the cavity results in sudden changes of the resistance. The device can still be deemed functional

up to this point. However, continued stretching can cause the gap between the connector and the channel in the encapsulant to become large enough to break the LM trace. Here, part of the LM remains adhered to the connector electrode and part adheres to the silicone channel. If this gap becomes large enough, the LM separates. When the device is relaxed and the LM contacts again, no electrical reconnection occurs due to the oxide layers. Sufficient mechanical force is needed to break this oxide and reconnect the trace. However, this does not happen spontaneously. Post mortem analysis was performed on samples cyclically tested to 100% strain after 100 000 cycles by removing the top encapsulant layer, exposing the solid–liquid interconnection and LM trace. The LM around the connector interface has significantly darkened and behaves more like a paste than a fluid. This deposit can be seen anywhere around the connector where delamination has occurred and where LM was able to flow in. Subsequent mechanical shearing over thousands of cycles caused the LM to turn into a more viscous mixture of LM and rigid particles. This change in rheology is what ultimately causes the disconnection. The micrographs in Figure 3g shows the LM along the traces, which retain their morphology and chemistry. The bottom micrograph in Figure 3g shows the darkened paste-like material on the connector, where an increased level of oxidation is seen as well as carbon and silicon, most likely originating from the encapsulant, as shown in the EDX spectra in Figure S3.

Adding strain relief (SR) is a method to reduce the amount of stress concentrated on the connector edge. In this work, strain relief is added by drop-casting a region of a higher Young's modulus material (than the encapsulant) over the interconnect prior to overmolding (Figure 4a). Drop-casting of the strain relief was done by applying 1 mL of Dragon skin 10 Fast (DS10) using a disposable luer-lock syringe immediately after mixing the DS10 (60 s at 2000 rpm in Hauschild speedmixer DAC400). Positioning of the drop was done by eye, directly over the LM to solid metal interface at the connector. The same is done on the opposite side after the liquid metal channels have been sprayed. This reduces the material mismatch at the connector and reduces the stress at the edge by effectively isolating the connector from the strain. The ideal transition would be a smooth transition in Young's modulus from flexible to stretchable [32] (Figure S4). However, this method provides a stepped transition, reducing the material mismatch at the interconnection significantly. Important to note is that sufficient adhesion between the connector and the SR is needed, as well as adhesion between the SR and the encapsulant. Here, DS10 was used as a strain relief because of its compatibility with the EF30 encapsulant and its higher Young's modulus. The DS10 has significantly better adhesion to the connector, which must also be taken into account. It will also aid in reducing the delamination of the connector. A comparison of the adhesion of both materials is added in (Figure S5).

Next, cyclic stretch testing was performed between 0% and 50% strain at an average cycle rate of 0.5 cycles/s for sample with and without strain relief. Notably, no failures were observed at this strain within 1 000 000 cycles for both groups. However, Figure 4b shows the average resistance increase of the samples with strain relief is significantly lower than without strain relief, indicating that the increase is largely caused at the interface. Furthermore, when looking at the resistance increase of a sample

without strain relief, it is apparent that there are large fluctuations in the resistance during the test, caused by the liquid metal flow at the connector when delamination occurs. Still, this delamination does not become large enough to cause a full disconnect. The samples with strain relief have a much more stable and predictable response throughout the tests. No large fluctuations were observed and the small bands indicate small sample to sample variations. Furthermore, all samples show a large resistance increase in the first 100 cycles, after which the resistance increase gradually levels off.

In the next stage, a harsher cyclic stretch test up to 100% strain was performed. Here, open circuit failures did occur and the resulting Kaplan–Meier survival function is shown in Figure 4c. For each sample, a distinction is made between the measurements at 0% stretch (solid line) and 100% stretch (dotted line). This means, a sample can be FAILED (resistance larger than 10 times the initial) at 100% strain, but still be connected at 0% strain due to the unique fluid nature of the LM. The graph shows a clear improvement in survivability for the samples with DS10 as strain relief. The samples without SR show a high early mortality rate, with almost 50% of the samples failing in the first 1000 cycles and dropping to 16% survival by 100 000 cycles. Devices with SR extend their lifetime by surviving up to 10 000 cycles before early mortality occurs. After this, about 50% of the samples survive beyond 100 000 cycles. A log-rank test, as performed in JMP-Pro, confirms the difference between the groups with a resulting p-value of 0.0202. The FEM simulation in Figure 4d illustrates how the area around the connector is isolated from strain when stretched to 50% strain. Without strain relief, there is a very large strain (max. logarithmic principal strain = 1.410) at the FPC connector edge due to the mechanical mismatch between the flexible connector and the stretchable encapsulant. Due to this high strain and the forces associated with it, the connector and encapsulant delaminate at this location, after which LM can flow into the cavity as shown in the degraded sample in Figure 4e. This is also the reason for the high amount of early failures, because delamination is instant. With DS10 strain relief, this strain is significantly reduced (max. logarithmic principal strain = 0.709) because the mismatch between the connector and DS10 modulus is lower. Consequently, no delamination and LM flow is seen in the degraded sample in Figure 4e. In the samples with strain relief, there is a color gradient along the wire, where the trace still has its original silver color in the strain relieved regions, confirming the reduced stretching in that location. Further, the connections often fail first at 100% strain but still remain functional when relaxed for some cycles before also failing. The X-ray images in Figure 4f confirm this. Samples without SR shows flowing of LM at the connector edge after 1000 cycles. There is a full disconnect between the trace and the connector pad after 10 000 cycles, which is even more significant after 100 000 cycles, as shown by the large gap between the electrode (yellow dashes) and LM trace (blue dashes). On the other hand, the X-ray of the sample with DS10 strain relief only shows significant flow at 100 000 cycles but no disconnection. SEM/EDX analysis on the samples with SR was not possible because of the strong adhesion of the DS10 region could not cleanly be separated at the connector interface. However, we expect the same elements to be present, but only the amount of material to be significantly reduced as visible by eye.

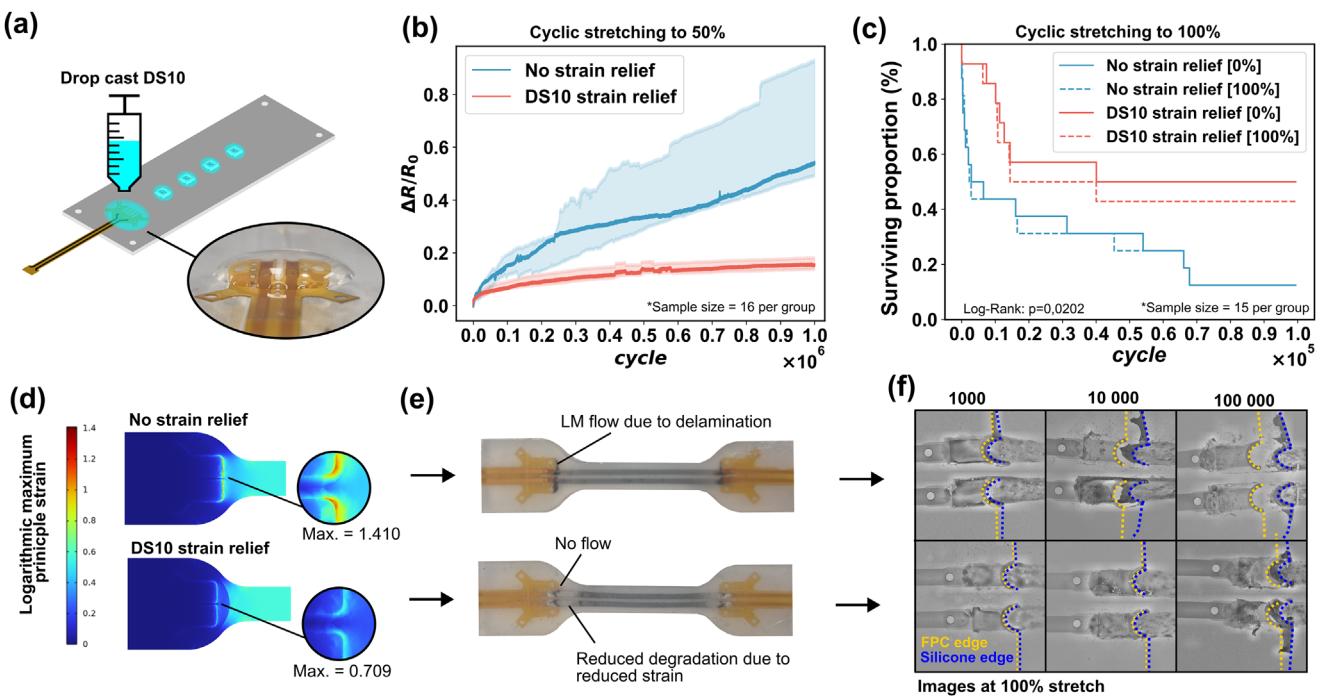


FIGURE 4 | (a) Additional production step for applying strain relief by drop casting DS10 over critical areas such as connectors and components. (b) Averaged resistance change with Q1 and Q3 errorbands in cyclic stretch testing up to 50% strain for samples with and without strain relief. Devices without strain relief have significant strain at the connector edge, which is significantly reduced with strain relief. (c) Kaplan–Meier survival curve of samples with and without strain relief in cyclic stretch testing up to 100% strain. A log-rank test with a p-value of 0.0202 confirms the difference between both groups. (d) FEM simulation of the Logarithmic maximum principal strain in a stretch test up to 50% strain for a device with and without strain relief. Zoomed images show the connector edge and the maximum logarithmic principal strain. (e) Images of degradation of samples at 100% strain after the stretch test from Figure 4b without (top) and with (bottom) strain relief. (f) X-Ray Tomography images of degradation of samples during the test from Figure 4c at different cycles without (top) and with (bottom) strain relief. Yellow dashes show the FPC connector edge. Blue dashes show the corresponding silicone edge and how it moved due to delamination.

4 | Strain Relief on Rigid Components

Here, the generalizability of the strain relief is tested. Instead of a flat and wide FPC ($\sim 10 \times 0.1$ mm), the strain relief method is verified on a stretchable device with a small cube-shaped ($2 \times 1 \times 0.5$ mm) rigid component. Figure 5a shows a device with an integrated resistor and LED stretched to ≈ 3 times its original length. The “0805 component” sample design from Figure 1a is used to investigate the efficacy of the SR on small integrated rigid components. SR is again applied by drop casting DS10 over both the component and connectors as indicated in Figure 5c. The voltage change in the initial strain cycle to 50% stretch was measured and is shown in Figure S7. The hypothesis is that the applied voltage will increase with strain to supply a constant current of 20 mA to the LED because of the increasing resistance of the connections. However, the increasing temperature of the device due to heating of the LED and its subsequent decreasing forward voltage at constant current causes a drop in measured voltage. Still, the effect of trace and contact resistance increase is visible in the upward curve on the loading cycle and the steeper drop in the unloading cycle.

The cyclic reliability of the devices was tested and compared for devices with and without SR. Stretching was performed up to 50% elongation but it must be noted that the actual stretch around the component is slightly larger due to the dogbone sample geometry. Before testing, the strain around the LED was simulated as shown

in Figure 5b. Similar to the flex-connector, the strain is highly concentrated at the sharp edges of the component at the interface from rigid to stretchable. Again, the (logarithmic) maximum principal strain at this edge is significantly reduced with SR (from 1.231 to 0.777 at 50% stretch with DS10 SR). The Kaplan–Meier survival curve in Figure 5d shows that the samples without strain relief all fail before 800 000 cycles at an almost constant failure rate. Conversely, only a single sample with SR failed after 750 000 cycles while the others remained functional beyond 2 000 000 cycles. An open circuit occurred as a result of delamination at the component. A log-rank test was again performed, resulting in a p-value of 0.0063. Most failed samples failed due to an open circuit, but a single sample without SR failed due to a short circuit at the LED. This is shown in Figure 5c, where LM has flowed next to the LED due to delamination with the silicone, causing a short circuit between the closely spaced connections. Further, we observed that after sample failure at maximum extension, no reconnection was made when relaxing the samples.

5 | Conclusion

While most of the research on LM-based devices focuses on showing stable performance of their material, production, etc., this work pushes beyond that region and up to failure. In doing so, it is demonstrated that the long-term mechanical reliability of liquid metal-based stretchable electronics is critically limited by

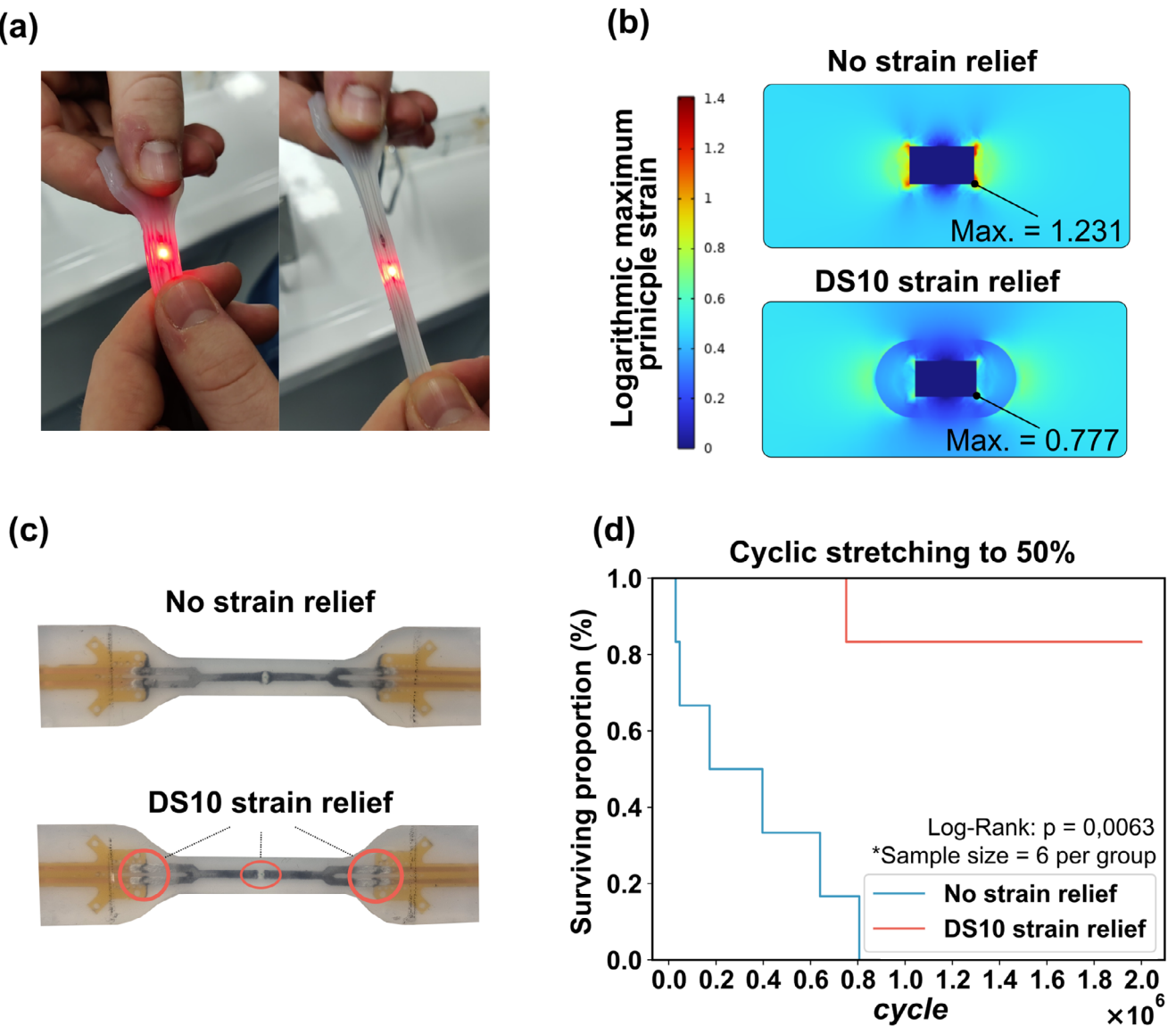


FIGURE 5 | (a) Demonstration of a device with an integrated resistor and LED with SR, which remains functional when stretched to more than three times the original size. (b) FEM simulated logarithmic principal maximum strain around the 0805 SMD component in a stretch test to 50% strain without (top) and with (bottom) strain relief. (c) Images of degraded samples from the test in Figure 5d after 2 000 000 cycles with indicated SR regions. (d) Survival curve of the “0805 component” LED devices in a cyclic stretch test up to 50% strain.

failures at the solid–liquid interface. Although secondary issues such as delamination, silicone rupture, and short circuits can be mitigated through process and connector design improvements, the dominant failure mode arises from stress concentration at the connector edge, leading to progressive delamination between the encapsulant and the flex-connector and eventual open-circuit behavior. By introducing strain relief around the connection with a higher modulus material, the interfacial stress was significantly reduced, which stabilized electrical performance and extended device lifetime under both moderate (50%) and high (100%) strain conditions. Moreover, the approach was validated on rigid-component assemblies, where strain relief enabled LED-integrated systems to operate reliably beyond two million cycles at 50% strain. These results demonstrate that targeted interface engineering is essential for achieving durable liquid metal stretchable interconnections. Ultimately, this work serves as a guideline for the sample design, test setup and method, and subsequent

analysis for identifying degradation and failure mechanisms in LM-based stretchable electronics.

Author Contributions

Lennert Purnal contributed to the conceptualization, investigation, data curation, methodology, formal analysis, and drafting of the manuscript; Maximilian Krack performed the batch fabrication and produced Figure 2; Parth Vinayakrao Sewlikar carried out the SEM/EDX investigations; Bart Ruttens conducted the X-ray investigations; Tom Hauffman and Iris De Graeve provided supervision; Wim Deferme contributed through supervision, review and editing, funding acquisition, and project administration; Michaël Daenen provided supervision, formal analysis, and review and editing of the original draft; and Monika Rai contributed through supervision, formal analysis, and review and editing of the original draft.

Acknowledgements

The authors want to thank Fonds Wetenschappelijke Onderzoek (FWO) for funding this work as part of the SBO project SUBLIME (S007423N). Further, the authors want to thank FWO and the Bijzonder Onderzoeks-fonds for providing personal funding to Maximilian Krack (1SH1C24N and BOF23INCENT17 respectively).

Conflicts of Interest

The authors declare no conflict of interest.

Data Availability Statement

The data that support the findings of this study are available from the corresponding author upon reasonable request.

References

1. L. Gillan, J. Hiltunen, M. H. Behfar, and K. Rönkä, "Advances in Design and Manufacture of Stretchable Electronics," *Japanese Journal of Applied Physics* 61, no. SE (2022): SE0804.
2. Q. Zhang, N. Li, Y. Song, et al., "Liquid Metal Sensors for Soft Robots," *Advanced Robotics Research* (2025): 202500057.
3. R. N. Sangma, S. Terryn, M. Krack, et al., "Recyclable and Self-Healing Stretchable Strain Sensor Based on Liquid Metal and Diels-Alder Polymer for Smart Wearable Applications," *IEEE Sensors Journal* (2025).
4. S. Jamalzadegan, S. Kim, N. Mohammad, et al., "Liquid Metal-Based Biosensors: Fundamentals and Applications," *Advanced Functional Materials* 34, no. 31 (2024): 2308173.
5. X. Li, G. Wu, C. Gao, R. Bao, and C. Pan, "Flexible Electronic Devices and Wearable Sensors Based on Liquid Metals," *MetalMat* 2, no. 1 (2025): e70000.
6. Y. Deng, F. Bu, Y. Wang, P. S. Chee, X. Liu, and C. Guan, "Stretchable Liquid Metal Based Biomedical Devices," *npj Flexible Electronics* 8, no. 1 (2024): 1–22.
7. Z. Lin, T. Li, S. Yang, B. Ji, and Z. Wang, "Revolutionizing Flexible Electronics with Liquid Metal Innovations," *Device* 2, no. 5 (2024): 100331.
8. M. D. Dickey, "Stretchable and Soft Electronics Using Liquid Metals," *Advanced Materials* 29, no. 27 (2017): 1606425.
9. M. Li, Y. Wu, L. Zhang, et al., "Liquid Metal-Based Electrical Interconnects and Interfaces with Excellent Stability and Reliability for Flexible Electronics," *Nanoscale* 11, no. 12 (2019): 5441–5449.
10. J. Ma, F. Krisnadi, M. Hou Vong, et al., "Shaping a Soft Future: Patterning Liquid Metals," *Advanced Materials* 35, no. 19 (2023): 2205196.
11. B. Yang, Z. Yang, and L. Tang, "Recent Progress in Fiber-Based Soft Electronics Enabled by Liquid Metal," *Frontiers in Bioengineering and Biotechnology* 11 (2023): 1178995.
12. Z. Kranz, E. Shafer, and A. M. Watson, "Strain Isolation for Flexible-to-Stretchable Electrical Interconnects," *FLEPS 2023 - IEEE Int. Conf. on Flexible and Printable Sensors and Systems* (IEEE, 2023).
13. B. Ping, G. Zhou, Z. Zhang, and R. Guo, "Liquid Metal Enabled Conformal Electronics," *Frontiers in Bioengineering and Biotechnology* 11 (2023): 111812.
14. S. Erlenbach, K. Mondal, J. Ma, et al., "Flexible-to-Stretchable Mechanical and Electrical Interconnects," *ACS Applied Materials and Interfaces* 15, no. 4 (2023): 6005–6012.
15. S. Nagels and W. Deferme, "Fabrication Approaches to Interconnect Based Devices for Stretchable Electronics: A Review," *Materials* 11, no. 3 (2018): 375.
16. L. Purnal, M. Rai, S. Vandervoort, et al., "Influence of Uniaxial Stretching on the Joule Effect-Induced Heating of Liquid Metal-Based Stretchable Electronic Devices," *IEEE Journal on Flexible Electronics* 4, no. 6 (2025): 234–241.
17. D. G. Marques, P. A. Lopes, A. T. De Almeida, C. Majidi, and M. Tavakoli, "Reliable Interfaces for EGaIn Multi-Layer Stretchable Circuits and Microelectronics," *Lab on a Chip* 19, no. 5 (2019): 897–906.
18. H. Kawakami, K. Nagatake, S. Ni, et al., "R2R-Based Continuous Production of Patterned and Multilayered Elastic Substrates with Liquid Metal Wiring for Stretchable Electronics," *Advanced Materials Technologies* 9, no. 17 (2024): 2400487.
19. *Liquid Wire* [Online], Available: <https://www.liquidwire.com/>.
20. C. Votzke, U. Daalkhajav, Y. Menguc, and M. L. Johnston, "3D-Printed Liquid Metal Interconnects for Stretchable Electronics," *IEEE Sensors Journal* 19, no. 10 (2019): 3832–3840.
21. D. Qi, K. Zhang, G. Tian, B. Jiang, and Y. Huang, "Stretchable Electronics Based on PDMS Substrates," *Advanced Materials* 33, no. 6 (2021): 2003155.
22. T. Kim, H. Lee, W. Jo, T. S. Kim, and S. Yoo, "Realizing Stretchable OLEDs: A Hybrid Platform Based on Rigid Island Arrays on a Stress-Relieving Bilayer Structure," *Advanced Materials Technologies* 5, no. 11 (2020): 2000494.
23. R. Moser, G. Kettlgruber, C. M. Siket, et al., "From Playroom to Lab: Tough Stretchable Electronics Analyzed with a Tabletop Tensile Tester Made from Toy-Bricks," *Advanced Science* 3, no. 4 (2016): 1500396.
24. M. S. Kim, S. Kim, J. Choi, et al., "Stretchable Printed Circuit Board Based on Leak-Free Liquid Metal Interconnection and Local Strain Control," *ACS Applied Materials and Interfaces* 14, no. 1 (2022): 1826–1837.
25. M. G. Kim, H. Alrowais, and O. Brand, "3D-Integrated and Multifunctional All-Soft Physical Microsystems Based on Liquid Metal for Electronic Skin Applications," *Advanced Electronic Materials* 4, no. 2 (2018): 1700434.
26. "ASTM D412-16R21 - Test Methods for Vulcanized Rubber and Thermoplastic Elastomers - Tension," West Conshohocken, PA, 5 Universidad Internacional Sek (2021).
27. S. Nagels, T. Vandenryt, and W. Deferme, "Interconnect, an Electronic Assembly and a Method for Manufacturing an Electronic Assembly," Hasselt Universiteit Interuniversitair Microelektronica Centrum vzw IMEC (2022).
28. M. Krack, R. N. Sangma, L. Purnal, et al., "Process and Property Assessment of Liquid Metal Spray Deposition Towards Scalable and Reliable Stretchable Electronics," *Scientific Reports* 15, no. 1 (2025): 35984.
29. K. B. Ozutemiz, J. Wissman, O. B. Ozdoganlar, and C. Majidi, "EGaIn-Metal Interfacing for Liquid Metal Circuitry and Microelectronics Integration," *Advanced Materials Interfaces* 5, no. 10 (2018): 1701596.
30. T. V. Neumann, B. Kara, Y. Sargolzaeiaval, et al., "Aerosol Spray Deposition of Liquid Metal and Elastomer Coatings for Rapid Processing of Stretchable Electronics," *Micromachines* 12, no. 2 (2021): 146.
31. D. Ahmad and R. M. Ajaj, "A Multiaxial Fracture of Ecoflex Skin with Different Shore Hardness for Morphing Wing Application," *Polymers* 15, no. 6 (2023): 1526.
32. Z. Wu, S. Zhang, A. Vorobyev, K. Gamstedt, K. Wu, C. Guo, and S. H. Jeong, "Seamless Modulus Gradient Structures for Highly Resilient, Stretchable System Integration," *Materials Today Physics* 4 (2018): 28–35.

Supporting Information

Additional supporting information can be found online in the Supporting Information section.

Supporting file